Damage accumulation in neon implanted silicon

E. Oliviero, S. Peripolli, L. Amaral, P. F. P. Fichtner, M. F. Beaufort, J. F. Barbot, and S. E. Donnelly

Citation: Journal of Applied Physics **100**, 043505 (2006); doi: 10.1063/1.2220644
View online: http://dx.doi.org/10.1063/1.2220644
View Table of Contents: http://scitation.aip.org/content/aip/journal/jap/100/4?ver=pdfcov
Published by the AIP Publishing

Damage accumulation in neon implanted silicon

E. Oliviero,[a] S. Peripolli, and L. Amaral
Instituto de Física, Universidade Federal do Rio Grande do Sul, Avenida Bento Gonçalves 9500, Caixa Postal 15051, 91501-970 Porto Alegre, Rio Grande do Sul, Brazil

P. F. P. Fichtner
Departamento de Metalurgia, Universidade Federal do Rio Grande do Sul, Avenida Bento Gonçalves 9500, Caixa Postal 15051, 90035-190 Porto Alegre, Rio Grande do Sul, Brazil

M. F. Beaufort and J. F. Barbot
Laboratoire de Métallurgie Physique UMR6630, Université de Poitiers, SP2MI, Boulevard Marie et Pierre Curie, BP30179, 86962 Futuroscope-Chasseneuil Cedex, France

S. E. Donnelly
Institute for Materials Research, University of Salford, Greater Manchester M5 4WT, United Kingdom

(Received 24 January 2006; accepted 27 May 2006; published online 18 August 2006)

Damage accumulation in neon-implanted silicon with fluences ranging from 5×10^{14} to 5×10^{16} Ne cm^{-2} has been studied in detail. As-implanted and annealed samples were investigated by Rutherford backscattering spectrometry under channeling conditions and by transmission electron microscopy in order to quantify and characterize the lattice damage. Wavelength dispersive spectrometry was used to obtain the relative neon content stored in the matrix. Implantation at room temperature leads to the amorphization of the silicon while a high density of nanosized bubbles is observed all along the ion distribution, forming a uniform and continuous layer for implantation temperatures higher than 250 °C. Clusters of interstitial defects are also present in the deeper part of the layer corresponding to the end of range of ions. After annealing, the samples implanted at temperatures below 250 °C present a polycrystalline structure with blisters at the surface while in the other samples coarsening of bubbles occurs and nanocavities are formed together with extended defects identified as {311} defects. The results are discussed in comparison to the case of helium-implanted silicon and in the light of radiation-enhanced diffusion. © *2006 American Institute of Physics*. [DOI: 10.1063/1.2220644]

I. INTRODUCTION

Understanding mechanisms of damage accumulation in semiconductors and developing strategies for the control of impurities are essential to the continued development of microelectronic devices. Indeed, the introduction of impurities is crucial in semiconductor device processing as the functionality of semiconductor materials depends largely on the controlled introduction of dopants, a step which nowadays generally involves ion implantation. Nevertheless, in addition to the introduction of dopants, implantation creates an excess of point defects, which, depending on implantation parameters, can coalesce to form extended defects (for a review of extended defects induced by ion implantation see Ref. 1). These defects may be electrically active and may create electronic levels localized in the band gap of the semiconductor (deep levels) and have been shown to strongly modify the electrical properties of the devices.[2,3] Thermal annealing, subsequent to ion implantation, is not only necessary to activate the dopant but also to remove the implantation-induced defects. Some extended defects have, however, been shown to be extremely stable and annealing at high temperature and/or for long times is necessary to remove them.[4]

Recently, ion implantation has received renewed interest with regard to the formation of nanocavities. In particular, nanosized cavities in silicon are usually formed by high fluence He ion implantation at ambient temperature. Due to its low solubility, He segregates in gas-vacancy complexes and, depending on implantation parameters such as energy and fluence, forms bubbles of a few nanometers in size. In 1986 Griffioen *et al.*[5] showed that during annealing at temperatures above 700 °C, bubbles grow (for an overview of the bubble growth mechanisms see Ref. 6) and He is released from bubbles due to its ability to permeate from inside the bubble to the matrix, leading ultimately to the formation of empty cavities (note that we will use "void" to refer to these defects, "bubbles" to refer to gas-filled cavities, and "cavity" to include both empty and gas-filled entities). Subsequently, research showed that these voids have clean internal surfaces (dangling bonds) that can trap metallic impurities.[7] Since then, cavities have been the subject of a considerable research effort and overviews of cavity formation and evolution in He implanted silicon have recently been published.[8,9] With the constant miniaturization of microelectronic devices, the purity requirements of semiconductors are becoming extremely severe. The density of metallic impurities in the active region of the device must be extremely low ($\leqslant10^{10}$ at. cm^{-3}).[10] To control these unwanted impurities, a gettering treatment is necessary and cavities have been shown to be a powerful technique to locally getter metallic

[a]Electronic mail: oliviero@if.ufrgs.br

impurities (proximity gettering, lateral gettering[11]). However, it has been shown that in some cases the formation of cavities is accompanied by the formation of extended defects[12] and that these defects can be stable even for long annealing times.[13] The discovery of this mechanism of defect formation gave rise to the deliberate use of cavities for strain relaxation: it has been shown that defects induced by the cavity formation can be used for very effective strain relaxation of pseudomorphic SiGe/Si heterostructures.[14–16] Cavities are also used in the process of "Smart Cut®" (H implantation[17] or combination of He and H implantation[18–20]) as a cutting tool for the production of silicon-on-insulator (SOI) structures. In addition, deep level transient spectroscopy (DLTS) measurements on diodes containing voids have shown the presence of deep levels localized near the middle of the band gap.[21,22] Thus these voids could also be used for the generation of recombination centers, for instance, to control charge carrier lifetime in the active region of silicon power devices. Ion implantation is also used to form buried layers in silicon.[23,24] Oxygen implantation has been studied for the development of Si-on-insulator substrates for Si-CMOS (complementary metal-oxide semiconductor) technology.[25,26] This process, known as separation by implanted oxygen (SIMOX), is already well developed and commercialized in Si-based SOI wafers. Implantation of Si or O at elevated temperatures in silicon leads to the formation of two distinct layers: a dislocation free near-surface layer and a layer of interstitial type defects (dislocation loops, stacking faults, {311}) located close to the region of ions' end of range.[27–29]

With reference to all of these aspects, a fundamental understanding of the buildup of radiation damage in silicon as well as its recovery is needed to advance technological applications. Recent studies have considered the effects of implantation temperature on characteristics of the He bubble system and on the damage accumulation.[30–34] The formation of bubbles affects the point defect fluxes in the matrix and therefore leads to the formation of quite distinct morphologies of extended defects (dislocation loops, rodlike and ribbonlike defects) compared to those occurring in the absence of cavity formation. The final defect morphology resulting from He implantation and annealing is a complex one which may consist of point defects and extended defects of both vacancy and interstitial types (the survival of vacancies and interstitials will depend on their separation during the implantation). The vacancy-type defects may or may not contain gas, and factors influencing the final defect morphology include the rate at which damage is introduced, the thermal and radiation-enhanced mobility of both gas and defects, and, in particular, the ability of the gas to permeate from cavities back into the matrix.

The extension of these studies that have largely involved helium to other inert gases should give insights into the damage accumulation processes in Si and a better understanding of the bubble formation mechanisms. Inert gas implantation (Ne, Kr, Ar, and Xe) in silicon has been already studied to some extent in the 1980s;[35–37] however, implantations were carried out at room temperature, leading to the amorphization of silicon samples. Under such conditions, neon implantation followed by annealing at 800 °C created arrays of dislocation loops and dipolelike structures,[38] polycrystalline regions, or dislocation networks, depending on the implanted fluence[39] and bubbles and microtwins in an epitaxially regrown layer.[36] Cullis *et al.*[35] reported the formation of bubbles after annealing together with a network of dislocations, with the bubbles often attached to dislocations. Elliman *et al.*[37] investigated the damage induced by MeV neon implantation, using implantation temperatures ranging between 20 and 300 °C. They observed by Rutherford backscattering spectrometry under channeling conditions (RBS/C) a drastic evolution of both the defect density and defect distribution with implantation temperature. However, there was no mention of cavity formation. Implantations at elevated temperatures in silicon with inert gases other than He (Refs. 30–34) have thus received scant attention.[40]

The purpose of the present study of the formation of cavities by neon implantation is to obtain a better understanding of damage accumulation and cavity formation in silicon. Neon differs from helium in at least two major respects: its introduction introduces significantly more concomitant radiation damage than that of helium and it is likely that Ne is unable to permeate from the bubbles—leading to gas-filled cavities rather than empty ones even after high-temperature annealing. Differences between the present work and previous results for helium should thus shed light on the importance of both the damage introduction rate [displacements per atom (dpa) per ion] and gas permeation. Results are compared with previous work and discussed in the light of bubble growth mechanisms.

II. EXPERIMENTAL METHODS

All the experiments were performed on commercial Czochralski-grown *n*-type (100) silicon wafers. The resistivity of the wafers was $1-2\ \Omega$ cm. These samples were implanted to fluences (ϕ) ranging from 5×10^{14} to 5×10^{16} cm^{-2} with 50 keV neon ions [$R_p=110$ nm and $\Delta R_p=43$ nm according to the stopping and range of ions in matter (SRIM) calculations[41]]. The beam flux was kept in the range of $(3-6)\times10^{12}$ ions cm^{-2} s^{-1}, since it was shown that changes in the implantation flux can strongly affect the accumulation of defects.[35,42] Some implantations were carried out at room temperature while others were performed at temperatures ranging from 100 up to 600 °C to avoid target amorphization. Anneals were performed in a vacuum of $\sim10^{-7}$ torr at temperatures ranging from 400 to 1100 °C for 30 min in a quartz tube within a tubular furnace.

As-implanted and annealed samples were investigated by RBS/C using an incident beam of 1.2 MeV $^4He^+$ from a 3 MV Tandetron in random or in ⟨100⟩ crystal directions. A scattering angle of 11° was used in order to have a good compromise between counts and depth resolution. The damage depth profiles were determined from the RBS spectra using the surface energy approximation outlined in Ref. 43.

The structure of the implantation damage was studied by plan-view (PV) transmission electron microscopy (TEM) and cross-sectional TEM (XTEM) using a JEOL 2010 operating at 200 kV. The samples were cut, glued, and then thinned using mechanical polishing and ion milling. In order

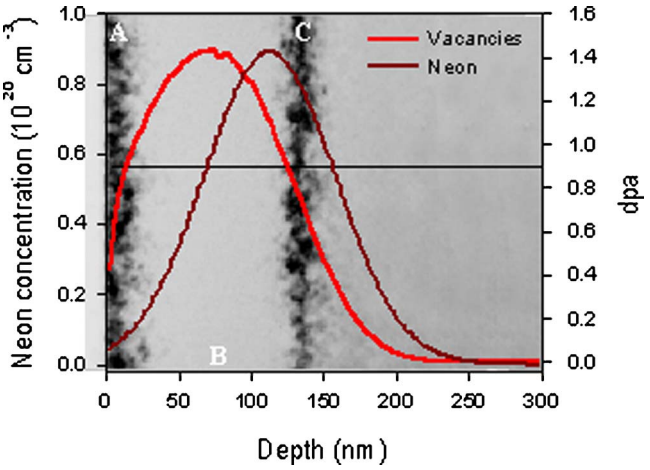

FIG. 1. (Color online) Cross-sectional TEM bright field micrograph of implanted silicon sample with 50 keV Ne at room temperature at 1×10^{15} Ne cm^{-2}. No additional anneal. Superposed, the neon concentration and the displacement per atom (dpa) derived from SRIM calculation.

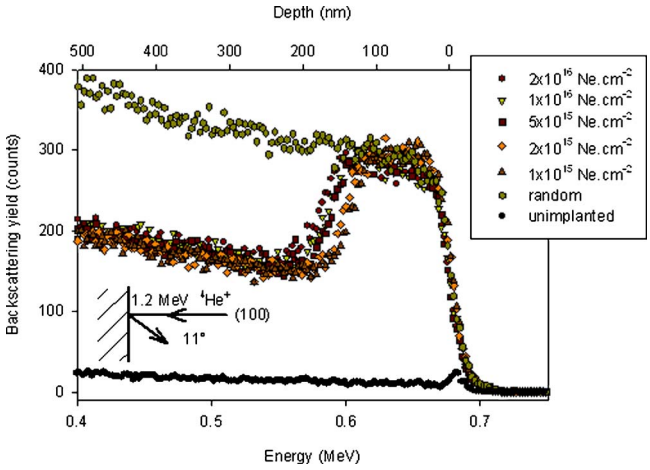

FIG. 2. (Color online) RBS/C spectra from (100) silicon samples implanted at room temperature with 50 keV Ne^+ ions at the indicated fluences.

to study cavities with minimal contrast from the unavoidable accompanying lattice damage, specimens were tilted from their ⟨110⟩ orientation by a few degrees in order to reduce diffraction effects. They were also imaged in underfocus and overfocus conditions to highlight the cavity edges with Fresnel contrast. In the following, S in the TEM images denotes the implanted surface of the sample.

The neon retention behavior was studied by wavelength dispersive spectrometry (WDS) by evaluating the intensity of characteristic x-ray emission of $K\alpha$ lines from Ne. Experimental data were acquired using a Cameca SX 50 electron microprobe equipped with four wavelength dispersive spectrometers. In analytical conditions, a 5 keV electron beam with a current of 100 nA was used. The diameter of the beam was 10 μm. Energy spectra were obtained using a thallium acid phthalate (TAP) crystal, with counting statistics of 30 s in steps of 0.489 eV. The WDS technique suffers from some limitations. In particular, it does not yield an absolute value for the Ne content. To overcome this limitation and to give a measure of relative Ne concentration, the neon content calculated by integrating the Gaussian peak centered on the Ne $K\alpha$ lines for the implant at RT with a fluence of 5×10^{16} Ne cm^{-2} will be our reference in the following.

III. RESULTS

A. As implanted

1. Implantations at room temperature

Neon implantations at room temperature (T_i=25 °C) in silicon lead to the formation of a continuous disordered zone. Figure 1 is a cross-sectional bright field TEM image of the damaged zone in silicon implanted at room temperature with $\phi=1\times10^{15}$ Ne cm^{-2}. The 150 nm wide damage layer centered at about 75 nm from the surface is made of three different regions. The central layer, denoted B, is a 100 nm wide amorphous layer. The two side regions denoted A and C, approximately 25 nm wide, are crystalline and exhibit black contrast that we ascribe to a high density of point defects or clusters thereof not resolvable by conventional TEM. No bubbles are observed even for the highest fluence ($\phi=5\times10^{16}$ Ne cm^{-2}). Either they are too small to be detected by Fresnel contrast or they are not formed. In Fig. 1, predictions of the Ne and vacancy concentration-depth profiles calculated by SRIM (Ref. 41) have been superimposed on the XTEM image to draw attention to the fact that the amorphous layer B is centered on the vacancy profile with the end of the layer close to R_p. Amorphization of silicon is found to occur for a dpa higher than 0.9. Considering this threshold, a fluence of as $\phi\leqslant5\times10^{14}$ Ne cm^{-2} should be implanted to avoid amorphization. However, for such low fluence only small clusters of interstitial defects are formed in the as-implanted sample and after annealing no bubbles are formed. Thus, the only method to form cavities and to avoid amorphization is to implant at elevated temperature. RBS/C spectra of samples implanted at room temperature for Ne fluences $1\times10^{15}\leqslant\phi\leqslant2\times10^{16}$ cm^{-2} are presented in Fig. 2. In all channeled spectra, a broad damage peak is observed starting at the Si surface with a height equal to that of randomly oriented Si, suggesting the formation of an amorphous layer. It should be noted that the disagreement with the TEM results showing a buried amorphous layer is due to RBS/C depth resolution limitations. The width of the amorphous layer is found to slightly increase with increasing implanted fluence with the growth occurring on the deeper side of the layer. In the WDS measurements in Fig. 3, a Gaussian peak centered on the neon $K\alpha$ lines is clearly observed for the implantation at room temperature with a fluence of $\phi=5\times10^{16}$ Ne cm^{-2}. This indicates that a certain amount of Ne is retained in the sample. As stated in the experimental procedure, the Ne content for the implant at RT with a fluence of $\phi=5\times10^{16}$ Ne cm^{-2} provides a calibration standard for comparative measurements of the Ne content to be further discussed.

2. Implantations at T_i=250 °C

To determine the minimum temperature at which amorphization does not occur under our implantation conditions, implantations at different temperatures (T_i) have been performed. Amorphization is avoided for an implantation tem-

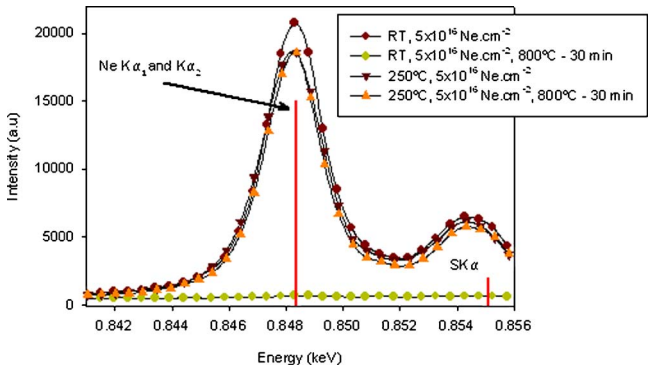

FIG. 3. (Color online) WDS spectra from (100) silicon samples implanted with 50 keV Ne^+ ions at the indicated fluences before and after annealing at 800 °C for 30 min.

perature in the range of 150 °C$\leqslant T_i \leqslant$250 °C. The increase of T_i enhances the dynamic annealing process (i.e., the recombination of self-interstitials and vacancies produced in the collision cascade), thus reducing the accumulated damage. However, it can be noted that for implantation temperatures higher than T_i=250 °C, no further significant changes are observed with regard to the damage accumulation. The effect of the fluence on the damage accumulation in samples implanted at T_i=250 °C is shown in Fig. 4. The accumulation exhibits a sigmoidal dependence with the maximum disorder at saturation under experimental conditions close to 90% at the damage peak. Full amorphization is thus no longer achieved. This is confirmed by TEM analysis using selected area diffraction that only shows the crystalline silicon pattern and no rings or additional halo pattern. The position of the damage peak appears to shift to greater depth with increasing fluence. The values are plotted in Fig. 4. Three different stages can be distinguished. At low damage level, i.e., for low fluences, stage I, no damage is detected. In stage II, in the region of superlinear accumulation, the damage is located at a depth of 125 nm, indicating the presence of defects close to the neon projected range R_p. Finally, in stage III, related to the saturation of the accumulation, the damage peak maximum is now found at about 200 nm which corresponds to $R_p+2\Delta R_p$, i.e., to the ions' end of range. The

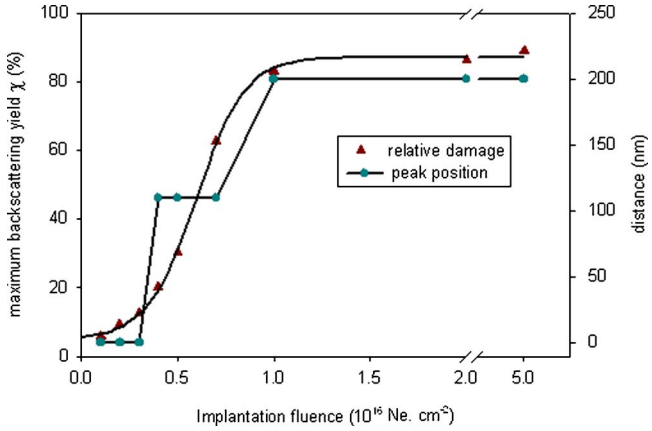

FIG. 4. (Color online) Maximum damage accumulation vs implanted fluence obtained from RBS/C spectra from (100) silicon samples implanted at 250 °C with 50 keV Ne^+ ions.

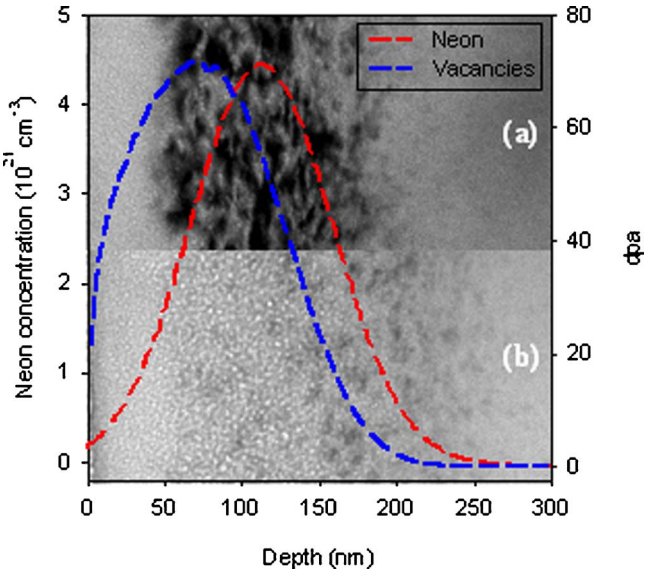

FIG. 5. (Color online) Cross-sectional TEM micrographs of implanted silicon samples with 50 keV Ne at 250 °C without additional anneal: at 7 $\times 10^{15}$ Ne cm^{-2} (a) and 5×10^{16} Ne cm^{-2} (b). Also shown are the superposed neon concentration and the dpa derived from SRIM calculation for fluence of 5×10^{16} Ne cm^{-2}.

XTEM observations show that for a fluence of ϕ=1 $\times 10^{15}$ Ne cm^{-2} only isolated bubbles are formed while for fluences higher than $\phi=7\times 10^{15}$ cm^{-2} a uniform and dense layer of bubbles is created [Fig. 5(a)]. Neon bubbles can be seen as white spots with a dark edge for underfocus condition. The bubbles are circular in shape with an average diameter of 3 nm. It was not possible to calculate precisely the bubble density; however, it appears to be dependent on the implanted fluence. The center of the bubble layer lies at 110 nm below the surface, corresponding to the projected range of the ions (R_p) calculated using SRIM simulation[41] and this layer is approximately 200 nm in width, i.e., close to $R_p+2\Delta R_p$ (the neon concentration and the dpa derived from SRIM calculation for fluence of 5×10^{16} Ne cm^{-2} are superposed in Fig. 5). Bubbles are thus found from the surface up to $R_p+2\Delta R_p$, i.e., all along the neon concentration profile. In all samples, no extended defects are observed but only dark contrast, certainly due to point defects or clusters of point defects. The front part, from the surface up to 50 nm, is always a region free of defect clusters. The defect clusters are found to be localized on the bubble band [Fig. 5(a)] for implantation at fluences $\phi\leqslant 7\times 10^{15}$ Ne cm^{-2} while they lie from 50 up to 300 nm from the surface for the other fluences [Fig. 5(b)], with the higher concentration at about 200 nm, i.e., at $R_p+2\Delta R_p$ corresponding to the peak in the RBS/C spectra. The WDS analysis (Fig. 3) of the samples implanted at T_i=250 °C shows that the increase of the implantation temperature to T_i=250 °C does not modify the neon retention behavior. A reduction of less than 5% of the retained neon is found in comparison to room temperature implantation, which is within the experimental uncertainties.

B. After annealing (800 °C for 30 min)

1. Implantations at room temperature and annealing

After annealing at 800 °C for 30 min, the amorphous layer formed during implantation at room temperature has

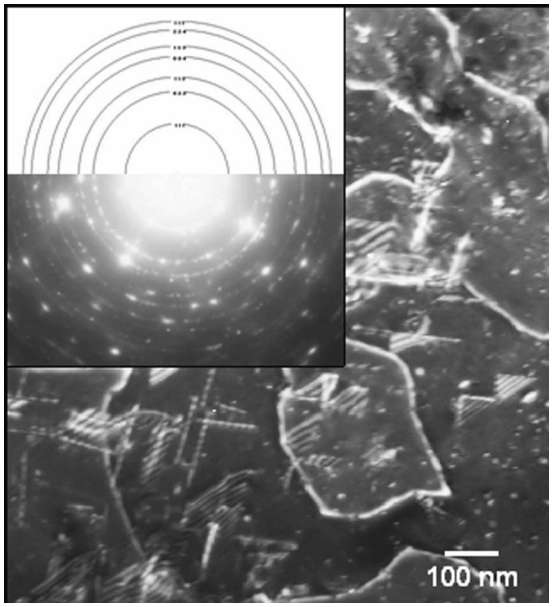

FIG. 6. Plan view TEM micrograph of implanted silicon sample with 50 keV Ne at room temperature at 5×10^{16} Ne cm^{-2} and annealed at 800 °C for 30 min.

recrystallized substantially. Plan-view TEM observations (Fig. 6) showed that the regrown damage layer contained mainly Si polycrystals. The residual lattice defects formed during the recrystallization seem to be principally stacking faults. Weak streaking in diffraction patterns indicated that some stacking faults occur near the final layer/matrix interface. It should be noted also that flaking/cratering of the implanted surface has occurred as observed by optical microscopy. A plan-view TEM micrograph of a flaked sample is shown in Fig. 6. In this case no bubbles are observed. The WDS measurements (Fig. 3) show that the neon is not retained in the sample after RT implantation followed by annealing at 800 °C for 30 min which is consistent with the fact that considerable exfoliation of the surface has occurred. Such neon release was also observed after annealing at 1100 °C for 15 s and craters were formed at the implanted surface.[44]

2. Implantations at T_i=250 °C and annealing

Upon annealing the bubbles grow significantly (Fig. 7), forming a 250 nm wide layer from the implanted surface. For the lowest fluence, $\phi=1\times10^{15}$ cm^{-2}, the density of bubbles of approximately 10 nm (±2 nm) in diameter has been estimated close to $(3-4)\times10^{15}$ cm^{-3}. At higher fluences, two different regions can be distinguished. From the surface up to 50 nm, small bubbles of 1–2 nm are observed. Their density is roughly constant, $(3-4)\times10^{16}$ cm^{-3}, for fluences up to $\phi=2\times10^{16}$ Ne cm^{-2} and drastically increases up to about $(1-2)\times10^{17}$ cm^{-3}, for $\phi=5\times10^{16}$ Ne cm^{-2}. Then, from 50 up to 250 nm larger bubbles are observed. Their mean diameter increases with the fluence, from 11 nm (±2 nm) for $\phi=7\times10^{15}$ Ne cm^{-2} up to 16 nm (±2 nm) for $\phi=5\times10^{16}$ Ne cm^{-2}. Their density is also found to increase with increasing fluence from 1×10^{16} to $(7-8)\times10^{16}$ cm^{-3}. The 50 nm wide tiny bubble band corresponds to the zone

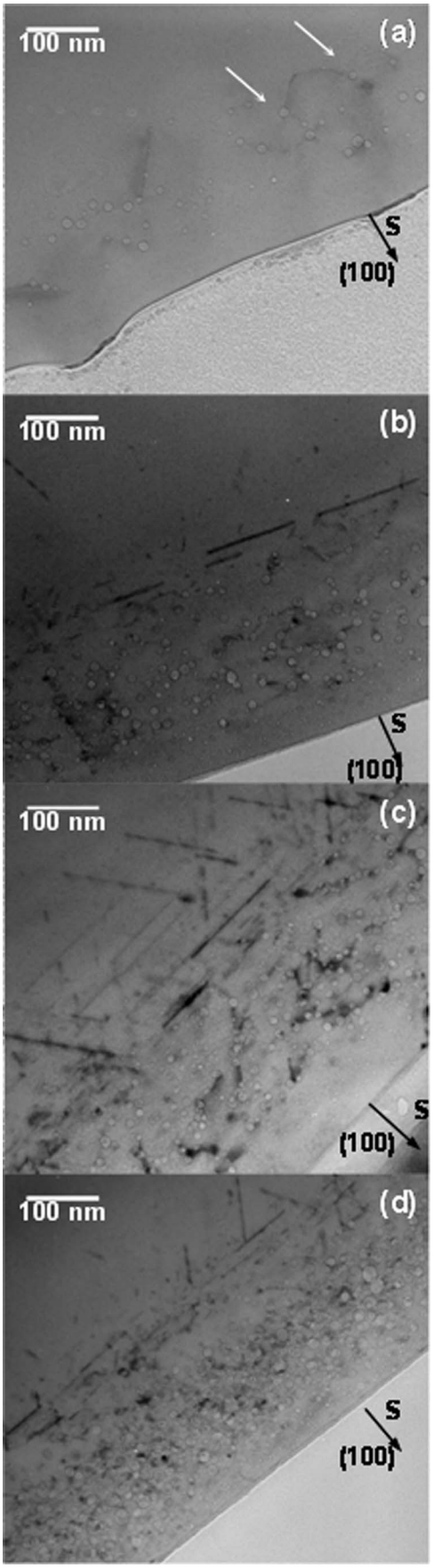

FIG. 7. Cross-sectional TEM micrographs of implanted silicon samples with 50 keV Ne at 250 °C: at 1×10^{15} Ne cm^{-2} (a), at 1×10^{16} Ne cm^{-2} (b), at 2×10^{16} Ne cm^{-2} (c), and at 5×10^{16} Ne cm^{-2} (d) and annealed at 800 °C for 30 min. Kinematical diffraction condition: underfocus.

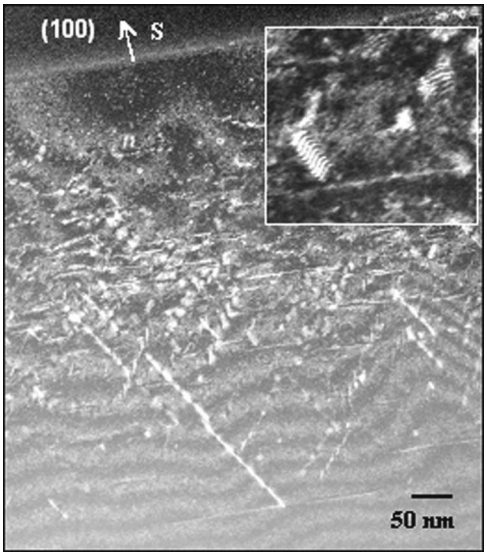

FIG. 8. Cross-sectional TEM weak beam dark field image of implanted silicon sample with 50 keV Ne at Ti=250 °C at 5×10^{16} Ne cm^{-2} and annealed at 800 °C for 30 min.

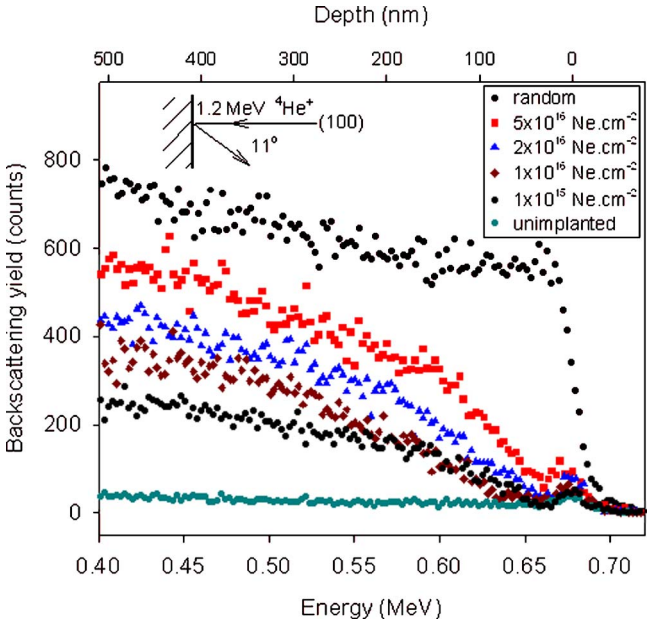

FIG. 9. (Color online) RBS/C spectra from (100) silicon samples implanted at 250 °C with 50 keV Ne$^+$ ions at the indicated fluences and annealed at 800 °C for 30 min.

which was free of interstitial clusters in the as-implanted sample. During implantation, the surface acts as a sink for interstitials. The same phenomenon can occur with vacancies during growth of bubbles, i.e., during annealing. The formation of tiny bubbles in the 50 nm front region can be explained by a limited Ostwald ripening: the proximity of the surface inhibits the growth of bubbles since it is acting as a sink for vacancies. No faceting of the bubbles is observed. The other effect of annealing on the damage layer is the agglomeration of interstitials leading to the formation of extended defects. For fluences $\phi \geqslant 7\times10^{15}$ Ne cm^{-2}, a high density of long defects extended in ⟨110⟩ directions is now observed (Figs. 7 and 8) beyond the bubble layer from 250 nm (at the ions end of range) up to deep in the bulk. These elongated defects lying on {113} planes have lengths ranging from 30 to 200 nm and they have been identified as {311} or "rodlike" defects. The dark field image in Fig. 8 shows that small defects are also present in the bubble layer. Objects exhibiting a fringe contrast are also observed in the vicinity of the bubble band (see the inset in Fig. 8) and are identified as ribbonlike defects. The latter are known to be the result of the growth of rodlike defects under electron irradiation.[45,46] They are two-dimensional interstitial platelets and can be seen as interstitial-type dislocation loops lying on {311} planes in contrast to perfect loops or Frank loops that lie on {111} planes. They have been observed in the case of helium implantation in silicon at high temperature.[31,32] In all samples, some dislocation networks are observed within the bubble layer. The dislocations seem to be attached to bubbles [see, for example, Fig. 7(a)].

Figure 9 shows the RBS/C spectra for the annealed samples. The damage accumulation is found to gradually increase from the surface to deep in the bulk. In contrast to what is observed for the as-implanted sample, the damage is no longer concentrated in a well-defined region but is more homogeneously distributed.

The WDS measurements show no changes in the neon content after annealing at 800 °C for 30 min.

IV. DISCUSSION

A. Amorphization—recrystallization

At implantation fluences greater than 5×10^{14} Ne cm^{-2}, Ne implantation at room temperature produces a multilayer structure: an amorphous layer surrounded by crystalline zones containing point defects. The formation of amorphous silicon by ion implantation depends on the kinetics of damage accumulation, which is governed by the competition between the damage generation and its annihilation (dynamic annealing). Amorphization occurs when the free energy of the damaged crystalline phase is higher than that of the amorphous phase.[47] In Fig. 1, it is clear that the amorphous layer is centered on the most heavily damaged region (maximum dpa), where the nuclear deposition is maximum. This indicates that the ion-beam induced amorphization occurred initially at this region. The thickness of amorphous layer increases then with the implantation fluence. Growth of the amorphous layer occurs by a layer-by-layer mechanism with relatively sharp interfacial transition regions, leading at the end of implantation to the observed buried layer. This was already observed by *in situ* RBS measurements in MeV Si$^+$ ions implantation in silicon single crystal at room temperature[48] where the amorphous layer was observed to grow towards both the surface and bulk. In the RBS spectra, even if it is not possible to distinguish between a highly damaged layer and an amorphous layer, the thickness of the amorphous layer formed at room temperature increases with fluence toward the bulk. Indeed, as observed in the TEM image (Fig. 1), the front part is already highly damaged at the lower fluence. The implantation energy used is relatively low so that the start of the amorphous zone is already very

close to the surface. Thus we only observed the increase of the amorphous layer toward the bulk. It should be noted that a very fast evolution occurs around the threshold fluence for full amorphization (superlinear damage accumulation[47]). During annealing at 800 °C for 30 min, the amorphous layer recrystallizes but leads to the formation of a polycrystalline layer containing a high density of extended defects. Usually, annealing of an ion-beam induced amorphous layer occurs by layer-by-layer solid phase epitaxial growth[49] (SPEG) and results in a low defect density in the recrystallized volume. When the amorphous layer extends to the surface, the defects forming at the amorphous/crystalline (a/c) interface are swept at the same time that the recrystallization advances up to the surface, leaving defects only behind the initial a/c interface.[50] In the case of buried amorphous layer, defects are also found along the meeting plane of the two regrowth fronts.[24,51] In our case, the residual defect structure is completely different and we propose a model for the recrystallization of the buried amorphous layer formed by Ne implantation, illustrated schematically in Fig. 10. It is likely that at the beginning of the anneal, SPEG initiates and epitaxial regrowth fronts advance both from the matrix and also from the near-surface layer [Fig. 10(b)]. Ne is thought to have a low mobility in silicon so that no diffusion is expected at the temperature of annealing used. However, Ne atoms may be swept by the advancing recrystallization front, leading to "recrystallization-enhanced segregation" and to a narrower/sharper Ne distribution, resulting in the agglomeration of Ne into bubbles [Fig. 10(c)]. When the moving a/c interface encounters the highest implanted gas concentrations, the strain induced by the bubbles breaks locally the regrowth symmetry [Fig. 10(d)]. The large bubbles formed at the a/c interface may have the effect of pinning the interface and preventing any further motion so that the amorphous layer does not get any smaller. However, at 800 °C, the temperature is high enough for random nucleation and growth (RNG) to occur (activation energy=4.0 eV) in the amorphous region and this gives rise to polycrystalline Si full of stacking faults. Such RNG recrystallization process was observed to happen in Si implanted (and amorphized) with 200 keV Xe.[52] The formation of polycrystals is accompanied by the accumulation of lattice defects that degrade the regrowing layer and lead to the formation of the observed defects. At the same time, Ne bubbles continue to grow and finally lead to flaking and exfoliation of the surface resulting in loss of the neon and formation of large irregular craters at the implanted surface [Fig. 10(e)]. The presence of inert gas in the silicon matrix during its recrystallization is shown to strongly influence the process. In Ar-implanted silicon it has been suggested that the large quantity of Ar present in a damaged Si layer is able to suppress the recrystallization of the layer.[35,53] In SiC, the presence of a high concentration of helium leads to the formation of different polytypes in the recrystallized area.[54]

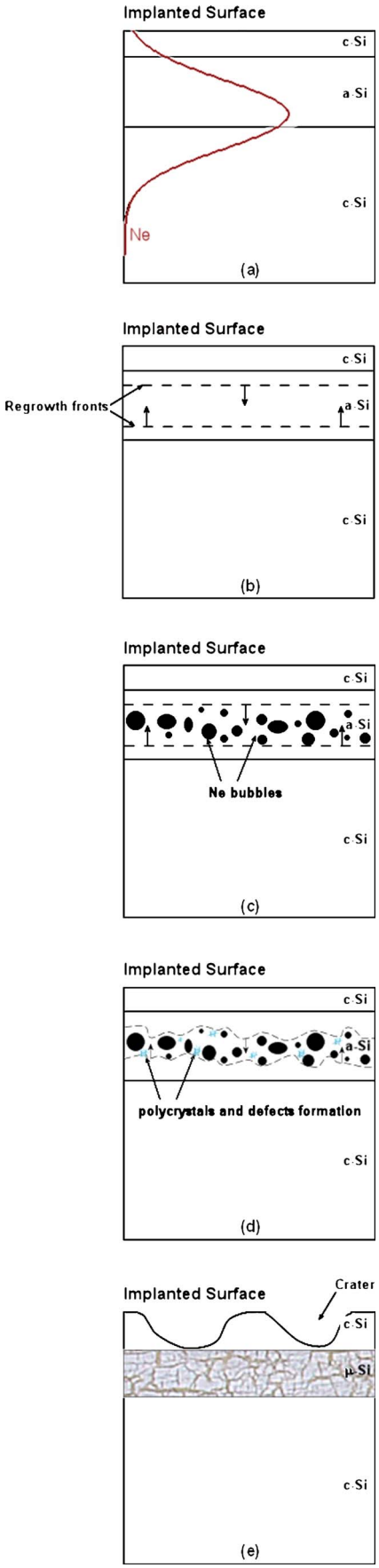

FIG. 10. (Color online) Model of the SPEG process of Ne implanted silicon as implanted (a), initialization of the SPEG process during annealing (b), formation of neon bubbles (c), SPEG stopped and polycrystals formation (d), residual defects after annealing (e).

B. Neon bubbles

Implantation at 250 °C using 50 keV Ne^+ avoids amorphization and produces small bubbles all over the ion distri-

bution. At low fluences, from $\phi=1\times10^{15}$ up to 5×10^{15} Ne cm^{-2}, only a small number of bubbles are formed and are randomly distributed. Such a bubble distribution does not correlate with what could be expected from the Ne distribution obtain by SRIM calculations and thus Ne movement is inferred. Although it is thought that Ne is not thermally mobile at 250 °C radiation-enhanced diffusion of mobile species involving Ne atoms over large distances (some tens of nanometers) must occur during implantation. The threshold neon concentration is thus locally reached, leading to the formation of stable bubble nuclei (probably Ne_nV_m clusters) and then to the formation of isolated bubbles. With increasing fluence, the bubble density increases leading at high fluences to a three-layer structure depending on the neon concentration. At $\phi=5\times10^{16}$ cm^{-2} a larger density of bubbles is observed in the central region ($R_p\pm\Delta R_p$) than in the two side layers. In the case of helium implantation at room temperature in Si, it is generally admitted that the limiting parameter for bubble formation is the local concentration[55] of helium around 3.5×10^{20} He cm^{-3}. Implantation above the threshold fluence for bubble formation ($\phi\geqslant10^{16}$ He cm^{-2})[56,57] leads to the formation of a well defined bubble layer in the region where the helium concentration is higher than the threshold concentration. Bubbles are observed in a buried layer, i.e., no bubbles are observed close to the surface where the helium concentration is low. However, experiments at implant temperature $T_i=200$ °C have shown the presence of few isolated bubbles close to the surface at high fluence[31,32] and might be attributed to the relocalization of helium or to He_nV_m or bubble migration. This phenomenon involving radiation-enhanced diffusion thus appears to be more significant in the case of neon implantation than in the helium case despite the assumed lower thermal mobility of neon atoms. Unfortunately, no diffusion data for neon in silicon are available in the literature. According to SRIM calculations for implantation in silicon, a 50 keV neon ion produces five times more Frenkel defects than a helium atom even if only a few percent will survive the displacement cascade recombination (~3% for low helium fluences[58]). The observed radiation-induced mobility of the neon atoms is thus almost certainly due to the greater dpa rate during neon implantation. The mobile entity may be either individual Ne atoms or Ne-vacancy complexes. When implanting He with fluences close to the threshold fluence, diluted system, characterized by heterogeneous growth of bubbles, platelike structures, and stress related defects (dislocation loops), can be observed.[12,59] This kind of system originates from a lack in vacancies that induces overpressurized states. In neon implantation this does not occur. No intermediate step is observed between a system with no bubble nucleation and a system of few bubbles in equilibrium distributed all along the neon distribution. The threshold fluence for bubble nucleation is thus found to be $\phi=1\times10^{15}$ Ne cm^{-2} at the implantation temperature, energy, and flux used. However, no local concentration threshold for neon implantation can be deduced since even for very low concentration values close to the surface or at the end of range of the ions, bubbles are formed for fluences close to the threshold fluence due to the relocation of the neon atom by radiation-enhanced diffusion. When the threshold fluence to form bubbles is reached, the number of vacancies available is already high and no overpressurized bubbles are formed. After annealing at 800 °C, bubbles are found to grow and the WDS measurements indicate the complete retention of the neon content. This differs from the helium/silicon system where helium is able to leave the cavity by a permeation process ($E_a=1.7$ eV). Therefore, when bubble growth occurs in the helium/silicon system, it leads to the formation of cavities. Two growth mechanisms are generally considered:[6] migration and coalescence and Oswald ripening although other growth mechanisms have been proposed in specific cases.[12] The role of gas in the growth of the cavities remains unclear. In this study of the Ne/silicon system we clearly show that the retention of gas does not impede bubble growth although it may have an effect on surface energy minimization processes within cavities since no faceting of the bubbles is observed. Alternatively, the presence of impurities has been shown to impede the faceting of bubbles.[60] Clearly, more detailed work is needed to settle this point.

Further investigations on the formation of Ne bubbles during implantation and their evolution after annealing are in progress for a better determination of the growth mechanism.

C. Damage accumulation

Three different damage accumulation regimes, depending on the fluence, are distinguished when implanting Ne at $T_i=250$ °C. At low damage level, i.e., in the low fluence range, stage I, no damage is detected because the concentration of defects is below the detection limit of both TEM and RBS techniques. In stage II, in the region of superlinear accumulation, point defects or clusters of point defects are located at a depth of 125 nm, i.e., on the bubble band. Upon annealing at 800 °C these defects annihilate and only dislocation networks are observed within the bubble layer. In stage III, related to the saturation of the accumulation, the damage peak maximum is found at about 200 nm which corresponds to $R_p+2\Delta R_p$, i.e., to the ions' end of range. After annealing, {311} defects and ribbonlike defects are formed beyond the bubble layer. In theses systems, vacancies are stored in the bubbles while interstitials are stored in clusters. The morphology of the resulting defects observed after annealing depends on the location of the interstitial clusters. When there is a larger separation of interstitials and vacancies, interstitials cluster in more complex defects such as {311} defects. If the clusters are located in the bubble layer, then a strong interaction with bubbles leads to strong annihilation, resulting in a low density of bubbles and nearly no extended defects. In the case of He implantation at room temperature, in the keV energy range, small bubbles and clusters of interstitials are formed in the same layer. After subsequent annealing at 700 °C or higher a well-defined bubble layer, free of extended defects, is formed. When implanting at 200 °C helium implantation leads to bubbles and clusters of point defects lying in a layer below the surface[31] and after annealing no extended defects are observed. For MeV implantation at high fluence, where the spatial separation of the vacancy and the interstitial excesses is larger, the

point defect clusters found in the as-implanted sample evolve to extended defects during annealing.[13] This points out the significance of the separation of interstitial and vacancies, a phenomenon that allows the accumulation of damage by preventing the recombination of Frenkel pairs. This mechanism involves the spatial separation of Frenkel defects.[61,62] Interstitial-vacancy pairs are created during irradiation as a result of atomic displacements. The momentum transferred to the interstitial will on average have a nonzero component along the direction of the incident ion. This leads to a spatial separation between the interstitial and vacancy defects with the interstitials having a deeper distribution profile. However, since the spatially correlated Frenkel pairs readily recombine,[59] only the excess or uncorrelated defects are left to contribute to residual damage. Thermal diffusion of defects will change the excess concentrations, especially near the interface between the excess vacancies and interstitials. But if vacancy clustering occurs such as bubble formation which traps the vacancies, it will form a less mobile defect and the excesses will be preserved. After annealing, the untrapped interstitials form the observed extended defects. In the case of neon implantation, neon being heavier than helium, the spatial separation is increased.

V. CONCLUSION

The effects of neon implantation in silicon have been investigated by a combination of RBS/C and TEM measurements. Neon implantation at room temperature at high fluence leads to amorphization and a multilayer structure is observed: an amorphous layer surrounded by crystalline zone regions containing point defects. After annealing at 800 °C for 30 min, recrystallization takes place resulting in a polycrystalline zone with stacking faults. A model for the recrystallization has been proposed considering the recrystallization-enhanced segregation of neon and the blistering of the implanted surface. For implantation at elevated temperature, it has been shown that a high density of bubbles is formed all along the Ne distribution. These bubbles grow after annealing at 800 °C for 30 min while extended defects (primarily {311} defects) are formed in the region of excess interstitials. The results have been discussed in comparison to the case of helium implantation and in the light of the radiation-enhanced diffusion. The two major differences between He and Ne implantation are the greater degree of damage produced by the Ne for the same energy and neon's inability to permeate though the silicon and leave bubbles on annealing at high temperature. These factors are both responsible for the observed differences in behavior.

ACKNOWLEDGMENTS

The authors would like to acknowledge M. Vasconcellos, Instituto de Fisica, UFRGS, for the WDS measurements and A. Bulla and C. Castello, Laboratorio de Implantaçao Ionica, for the implantations. One of the authors (S.E.D.) would like to thank the University of Poitiers for the invited Professor funding and Egide (www.egide.fr) for the Alliance project. This work was part of the CAPES-COFECUB program which the authors greatly acknowledge.

[1] K. S. Jones, in *Properties of Crystalline Silicon*, edited by R. Hull (EMIS, New York, 1999), Vol. 755, Chap. 20.
[2] F. Riedel, H. Hedemann, and W. Schröter, Nucl. Instrum. Methods Phys. Res. A **476**, 596 (2002).
[3] J. L. Benton, S. Libertino, D. J. Kringhoj, D. J. Eaglesham, J. M. Poate, and S. Coffa, J. Appl. Phys. **82**, 120 (1997).
[4] D. J. Eaglesham, P. A. Stolk, H.-J. Gossmann, T. E. Haynes, and J. M. Poate, Nucl. Instrum. Methods Phys. Res. B **106**, 191 (1995).
[5] C. C. Griffioen, J. H. Evans, P. C. de Jong, and A. van Veen, Nucl. Instrum. Methods Phys. Res. B **27**, 417 (1987).
[6] J. H. Evans, Nucl. Instrum. Methods Phys. Res. B **196**, 125 (2002).
[7] D. M. Follstaedt, S. M. Myers, C. A. Petersen, and J. W. Medernach, J. Electron. Mater. **25**, 157 (1996).
[8] V. Raineri, M. Saggio, and E. Rimini, J. Mater. Res. **15**, 1449 (2000).
[9] G. F. Cerofolini, F. Corni, S. Frabboni, C. Nobili, G. Ottaviani, and R. Tonini, Mater. Sci. Eng., R. **27**, 1 (2000).
[10] *International Technology Roadmap for Semiconductors*, 1999 Edition (Semiconductor Industry Association, Austin, TX, 1999).
[11] F. Roqueta, L. Ventura, J. J. Grob, and R. Jérisian, J. Appl. Phys. **88**, 5000 (2000).
[12] E. Oliviero, M. F. Beaufort, and J. F. Beaufort, J. Appl. Phys. **89**, 5332 (2000).
[13] M. F. Beaufort, E. Oliviero, H. Garem, S. Godey, E. Ntsoenzok, C. Blanchard, and J. F. Barbot, Philos. Mag. B **80**, 1975 (2000).
[14] H. Trinkaus, B. Hollander, S. Rongen, S. Mantl, H. J. Herzog, J. Kuchenbecker, and T. Hackbarth, Appl. Phys. Lett. **76**, 3552 (2000).
[15] M. Luysberg *et al.*, J. Appl. Phys. **92**, 4290 (2002).
[16] M. J. Mörschbächer *et al.*, Nucl. Instrum. Methods Phys. Res. B **219–220**, 703 (2004).
[17] M. Bruel, Mater. Res. Innovations **3**, 9 (1999).
[18] A. Agarwal, T. E. Haynes, V. C. Venezia, O. W. Holland, and D. J. Eaglesham, Appl. Phys. Lett. **72**, 1086 (1998).
[19] P. Nguyen, I. Cayrefourcq, K. K. Bourdelle, A. Boussagnol, E. Guiot, N. B. Mohamed, N. Sousbie, and T. Akatsu, J. Appl. Phys. **97**, 1 (2005).
[20] P. F. P. Fichtner *et al.*, (unpublished).
[21] V. Raineri, P. G. Fallica, and S. Libertino, J. Appl. Phys. **79**, 9012 (1996).
[22] N. Auriac and S. Martinuzzi, J. Phys.: Condens. Matter **14**, 13087 (2002).
[23] J. S. Williams, Mater. Sci. Eng., A **253**, 8 (1998).
[24] E. Oliviero, P. F. P. Fichtner, A. Gandy, S. E. Donnelly, M. F. Beaufort, and J. F. Barbot, (unpublished).
[25] S. Krause, M. Anc, and P. Roitman, MRS Bull. **23**, 25 (1998).
[26] K. Izumi, M. Doken, and H. Ariyoshi, Electron. Lett. **14**, 593 (1978).
[27] O. W. Holland, D. S. Zhou, and D. K. Thomas, Appl. Phys. Lett. **63**, 896 (1993).
[28] O. W. Holland, D. K. Thomas, and D. S. Zhou, Appl. Phys. Lett. **66**, 1892 (1995).
[29] D. Venables, K. S. Jones, and F. Namavar, Appl. Phys. Lett. **60**, 3147 (1992).
[30] E. Oliviero, M. L. David, M. F. Beaufort, J. F. Barbot, and A. van Veen, Appl. Phys. Lett. **81**, 3552 (2002).
[31] M. L. David, M. F. Beaufort, and J. F. Barbot, J. Appl. Phys. **93**, 1438 (2003).
[32] M. L. David *et al.*, Nucl. Instrum. Methods Phys. Res. B **198**, 83 (2002).
[33] D. L. da Silva, M. J. Mörschbächer, P. F. P. Fichtner, E. Oliviero, and M. Behar, Nucl. Instrum. Methods Phys. Res. B **219–220**, 713 (2004).
[34] D. L. da Silva, P. F. P. Fichtner, M. Behar, A. Peeva, R. Koegler, and W. Skorupa, Nucl. Instrum. Methods Phys. Res. B **190**, 756 (2002).
[35] A. G. Cullis, T. E. Seidel, and R. L. Meek, J. Appl. Phys. **48**, 5188 (1978).
[36] M. Wittmer, J. Roth, P. Revesz, and J. W. Mayer, J. Appl. Phys. **49**, 5207 (1978).
[37] R. G. Elliman, J. S. Williams, S. T. Johnson, and A. P. Pogany, Nucl. Instrum. Methods Phys. Res. B **15**, 439 (1986).
[38] D. J. Mazey, R. S. Nelson, and R. S. Barnes, Philos. Mag. **17**, 1145 (1968).
[39] S. M. Davidson and G. R. Booker, Radiat. Eff. **6**, 33 (1970).
[40] C. A. Cima, H. Boudinov, J. P. de Souza, Y. Suprun-Belevich, and P. F. P. Fichtner, J. Appl. Phys. **88**, 1771 (2000).
[41] J. F. Ziegler, J. P. Biersack, and U. Littmark, *The Stopping and Range of Ions in Solids* (Pergamon, New York, 1985).
[42] E. Oliviero, M. F. Beaufort, and J. F. Barbot, J. Appl. Phys. **90**, 1718 (2001).
[43] W. K. Chu, J. W. Mayer, and M. A. Nicolet, in *Backscattering Spectrometry* (Academic, New York, 1978).
[44] A. Markwitz, V. J. Kennedy, and H. Baumann, Nucl. Instrum. Methods

Phys. Res. B **206**, 179 (2003).
[45]C. A. Ferreira Lima and A. Howie, Philos. Mag. **34**, 1057 (1976).
[46]A. L. Aseev, L. I. Fedina, D. Hoehl, and H. Bartsch, *Clusters of Interstitial Atoms in Silicon and Germanium* (Akademie, Berlin, 1994).
[47]L. Pelaz, L. A. Marqués, and J. Barbolla, J. Appl. Phys. **96**, 5947 (2004).
[48]M. K. El-Ghor, O. W. Holland, C. W. White, and S. J. Pennycook, J. Mater. Res. **5**, 352 (1990).
[49]L. Csepregi, E. F. Kennedy, J. W. Mayer, and T. W. Sigmon, J. Appl. Phys. **49**, 3906 (1978).
[50]C. Bonafos, D. Mathiot, and A. Claverie, J. Appl. Phys. **83**, 3008 (1998).
[51]D. K. Sanada, M. Strathman, J. Washburn, C. W. Magee, M. Mäenpää, and G. R. Booker, Appl. Phys. Lett. **37**, 615 (1980).
[52]S. E. Donnelly and R. C. Birtcher (unpublished).
[53]P. Revesz, M. Wittmer, J. Roth, and J. W. Mayer, J. Appl. Phys. **49**, 5199 (1978).
[54]E. Oliviero, M. L. David, M. F. Beaufort, J. Nomgaudyte, L. Pranevicius, A. Declémy, and J. F. Barbot, J. Appl. Phys. **91**, 1179 (2002).
[55]V. Raineri, P. G. Fallica, G. Percolla, A. Battaglia, M. Barbagallo, and S. U. Campisano, J. Appl. Phys. **78**, 3727 (1995).
[56]S. M. Myers, D. M. Bishop, D. M. Follstaedt, H. J. Stein, and W. R. Wampler, Mater. Res. Soc. Symp. Proc. **283**, 549 (1993).
[57]A. V. Fedorov and A. van Veen, Comput. Mater. Sci. **9**, 309 (1998).
[58]B. G. Svensson, C. Jagadish, and J. S. Williams, Nucl. Instrum. Methods Phys. Res. B **80–81**, 582 (1993).
[59]P. F. P. Fichtner, J. R. Kaschny, R. A. Yankov, A. Mucklish, U. Kreissig, and W. Skorupa, Appl. Phys. Lett. **70**, 732 (1997).
[60]V. M. Vishnyakov, S. E. Donnelly, and G. Carter, J. Appl. Phys. **94**, 238 (2003).
[61]O. W. Holland, J. D. Budai, and B. Nielsen, Mater. Sci. Eng., A **253**, 240 (1998).
[62]P. Pellegrino, P. Lévêque, J. Wong-Leung, C. Jagadish, and B. G. Svensson, Appl. Phys. Lett. **78**, 3442 (2001).